

MULTI-SPACECRAFT OBSERVATIONS OF THE ROTATION AND NON-RADIAL MOTION
OF A CME FLUX ROPE CAUSING AN INTENSE GEOMAGNETIC STORM

YI A. LIU^{1,2}, YING D. LIU^{1,2}, HUIDONG HU¹, RUI WANG^{1,3}, AND XIAOWEI ZHAO^{1,2}

¹State Key Laboratory of Space Weather, National Space Science Center, Chinese Academy of Sciences, Beijing 100190, China; liuxying@swl.ac.cn

²University of Chinese Academy of Sciences, Beijing 100049, China

³W. W. Hansen Experimental Physics Laboratory, Stanford University, Stanford, CA, USA

ABSTRACT

We present an investigation of the rotation and non-radial motion of a coronal mass ejection (CME) from AR 12468 on 2015 December 16 using observations from *SDO*, *SOHO*, *STEREO A* and *Wind*. The EUV and HMI observations of the source region show that the associated magnetic flux rope (MFR) axis pointed to the east before the eruption. We use a nonlinear force-free field (NLFFF) extrapolation to determine the configuration of the coronal magnetic field and calculate the magnetic energy density distributions at different heights. The distribution of the magnetic energy density shows a strong gradient toward the northeast. The propagation direction of the CME from a Graduated Cylindrical Shell (GCS) modeling deviates from the radial direction of the source region by about 45° in longitude and about 30° in latitude, which is consistent with the gradient of the magnetic energy distribution around the AR. The MFR axis determined by the GCS modeling points southward, which has rotated

counterclockwise by about 95° compared with the orientation of the MFR in the low corona. The MFR reconstructed by a Grad-Shafranov (GS) method at 1 AU has almost the same orientation as the MFR from the GCS modeling, which indicates that the MFR rotation occurred in the low corona. It is the rotation of the MFR that caused the intense geomagnetic storm with the minimum D_{st} of -155 nT. These results suggest that the coronal magnetic field surrounding the MFR plays a crucial role in the MFR rotation and propagation direction.

Keywords: Sun: activity – Sun: coronal mass ejections(CMEs) – Sun: magnetic fields
– Sun: solar-terrestrial relations

1. INTRODUCTION

Coronal mass ejections (CMEs) are large-scale eruptions of plasma and magnetic field from the Sun and are a major driver of space weather effects. When propagating in the heliosphere, they are called interplanetary CMEs (ICMEs). A previous study suggests that at least 40% of CMEs observed by *SOHO*/LASCOS have a clear magnetic flux rope (MFR) structure (Vourlidas et al. 2013). In the low corona of the active region (AR), an MFR structure is manifested as a hot channel (HC), a high-temperature erupting structure seen in EUV observations (e.g., Cheng et al. 2013, 2014; Zhang et al. 2012). When a CME propagates from the Sun, it has a three-part structure in white-light observations: the white leading edge, core and dark cavity (Illing & Hundhausen 1985; Forsyth et al. 2006). The dark cavity is thought to be the MFR structure. The propagation direction of a CME MFR will determine whether it can arrive at Earth, and the orientation of a CME MFR will determine its southward magnetic field component at the Earth (e.g., Liu et al. 2010, 2016; Savani et al. 2015; Kilpua et al. 2012; Isavnin et al. 2014). Therefore, understanding the propagation and rotation of a CME MFR in the inner heliosphere is of crucial importance for space weather forecasting.

The propagation direction of a CME can deviate from the radial direction of the CME source region. The magnetic force produced by the coronal magnetic field plays an important role in CME propagation direction (MacQueen et al. 1986; Kilpua et al. 2009). Shen et al. (2011) and Gui et al. (2011) use the gradient of coronal magnetic energy density to explain the deflection of a CME in the low corona and suggest that the deflection is toward the region of the lower magnetic energy. Kay et al. (2013, 2015) develop a Forecasting CMEs Altered Trajectory (ForeCAT) model to predict CME trajectory. Heliospheric current sheets (HCSs) and coronal holes (CHs), which correspond to minimum and maximum energy regions on the solar surface, respectively, are important factors that can deflect CMEs (Kilpua et al. 2009; Gopalswamy et al. 2009; Liewer et al. 2015). Recent studies have demonstrated that CMEs can be deflected not only by the nearby large-scale structure, such as HCSs and CHs, but also can be channelled by the strong magnetic field in the CME source region itself (Möstl et al. 2015; Wang et al. 2015; Hu et al. 2017). CMEs can also change their propagation direction in interplanetary space by interacting with fast solar wind streams and other CMEs (e.g., Liu et al. 2014, 2016; Lugaz et al. 2012; Gopalswamy et al. 2001; Kataoka et al. 2015).

CME MFRs have been observed to rotate frequently (e.g., Vourlidas et al. 2011; Thompson et al. 2012; Liu et al. 2008b, 2010). Liu et al. (2010) suggest that a CME can exhibit a significant rotation during its propagation in the inner heliosphere by comparing the orientations of a CME MFR from the GCS modeling and the *in situ* reconstruction at 1 AU. MFR rotation in the corona has also been observed during CME eruption. Green et al. (2007) find that the direction of the MFR rotation is determined by the sign of helicity of the source region. For positive (negative) helicity, the MFR rotates clockwise (counterclockwise). This implies that the conversion of twist into writhe in a kink-unstable magnetic flux rope is a possible mechanism for the rotation (Kliem et al. 2012). As the orientation of MFR is a crucial parameter determining its geo-effectiveness, numerical simulations have been employed to understand the physical mechanism for the MFR rotation. Török & Kliem

(2003, 2005) find that vortex flows at the MFR foot points can drive a significant rotation (more than 90°) in an ideal MHD model. It suggests that the kink instability can cause the rotation. Using a similar model, Fan & Gibson (2004) obtain a larger rotation (almost 120°). Applying a breakout model in which the eruption starts with a developed MFR, Lynch et al. (2009) argue that the right-handed (left-handed) MFR rotates clockwise (counterclockwise) with a constant rate of about $30^\circ/R_\odot$, reaching a rotation angle of about 50° at a height of $3.5 R_\odot$. Based on observational or numerical studies, other mechanisms that cause MFR rotation have been suggested, such as reconnection with the ambient magnetic field (Cohen et al. 2010; Thompson 2011; Lugaz et al. 2011) and alignment with the heliosphere current sheet (Yurchyshyn 2008; Yurchyshyn et al. 2009). Interested readers are directed to Manchester et al. (2017) for a review of CME MFR rotation as well as deflection.

In the present paper, we investigate the propagation characteristics of the CME MFR from AR 12468 on 2015 December 16, using extreme ultraviolet, magnetogram, white-light and *in situ* observations from *SDO*, *SOHO*, *STEREO A*, and *Wind*. The paper is organized as follows. In section 2, we describe the solar source signatures from AIA and HMI observations, and reconstruct the configuration of the coronal magnetic field of the source region with a nonlinear force-free field (NLFFF) method and examine the magnetic energy density distribution at different heights. In sections 3 and 4, the Graduated Cylindrical Shell (GCS) method and Grad-Shafranov (GS) model are used to reconstruct the 3D structure of the MFR in the corona and at 1 AU to analyse the propagation and the rotation of the CME MFR. This study illustrates the important role of the coronal magnetic field around AR in the CME MFR rotation and propagation direction.

2. OBSERVATIONS OF THE SOURCE ACTIVE REGION

2.1. AIA and HMI Observations

The source region of the eruption event is AR 12468 (S15W15). It produced a halo-like CME and a C6.6 flare on 2015 December 16. The flare started at 8:25 UT and peaked at 9:00 UT. The source region was well covered by the Atmospheric Imaging Assembly (AIA; [Lemen et al. 2012](#)) and the Helioseismic and Magnetic Imager (HMI; [Schou et al. 2012](#)) on board the Solar Dynamics Observatory (SDO; [Pesnell et al. 2012](#)). AIA images the solar atmosphere at temperatures ranging from 0.06 MK to 20 MK through 10 passbands (7 EUV and 3 UV passbands). The image has a temporal cadence of 12 s (EUV) / 24 s (UV) and spatial resolution of $1''.2$. The HMI provides high time resolution magnetograms with a 45 s cadence and vector magnetic field data with a 12 min cadence. Its spatial resolution is $1''.0$.

Figure 1 shows *SDO*/AIA 131 Å and HMI observations of the source region before the eruption. The S-shaped hot channel marked by the red dotted curve in Figure 1(a) is regarded as the MFR producing the CME. The S-shape of the hot channel shows that the chirality of the MFR is likely right-handed (e.g. [Canfield et al. 1999](#); [Green & Kliem 2014](#)). The contours of the photospheric magnetic field along the line of sight from a *SDO*/ HMI magnetogram are overlaid on the EUV image in Figure 1(a). According to the contours, the MFR rooted in the strong negative polarity sunspot in the north and the strong positive polarity sunspot in the south. The orientation of the polarity inversion line (PIL) is almost from the west to the east. The axial field of the MFR comes from the positive polarity sunspot to the positive polarity sunspot, so the axis of MFR points to the east (marked by the arrow in Figure 1(b)). The angle between the orientation of the central part of the MFR and the horizontal direction (east) is about 5° . The MFR poloidal field comes out of the photosphere in the south and goes into the photosphere in the north of the PIL. For such a field configuration, the MFR should be right-handed. The MFR was aligned with the PIL before its eruption, which can be seen from the AIA EUV observations. At 8:00 UT, it started to expand and rise.

Figure 2 shows the EUV structures of the source region during the eruption of the MFR. The contours of *SDO*/HMI magnetograms are overlaid on the EUV images. The MFR from the *SDO*/AIA 131 Å image (Figure 1(a)) is indicated by the black dotted curve in Figure 2(a). The EUV loops overlying the MFR and the open EUV structures surrounding the MFR are marked in the AIA 171 Å images. At 8:00 UT, the MFR started to rise and then erupted in the AIA EUV observations. Figure 2(a)-(d) show that the EUV loops at the north of the MFR were pushed away by the CME MFR from 8:10 UT to 8:40 UT. The arrow pointing to the northeast in Figure 2(b) and Figure 2(c) shows the propagation direction of the disturbance along the open magnetic field lines. Therefore, we can roughly estimate that the CME MFR was propagating to the northeast.

2.2. Coronal Magnetic Field Reconstruction

We use an NLFFF method to understand the relation between the coronal magnetic field configuration and the propagation of the CME MFR in the low corona. The NLFFF method is proposed by Wheatland et al. (2000) and extended by Wiegelmann (2004) and Wiegelmann & Inhester (2010). We employ the NLFFF code, which has been optimized for application to *SDO*/HMI vector magnetograms (Wiegelmann et al. 2012), to extrapolate the coronal magnetic field from the observed vector magnetograms in a Cartesian domain. This extrapolation method works well by comparing the extrapolated magnetic fields with observed EUV structures as shown in previous studies (e.g., Vemareddy et al. 2013, 2016; Guo et al. 2010; Wang et al. 2014, 2015). Here, we bin the data to about 1".0 per pixel and adopt a computation domain of $512 \times 256 \times 160$ grids.

Figure 3 displays the comparison between the EUV images and the NLFFF extrapolation. The NLFFF extrapolation results of the source region are shown from different viewpoints. We use different colors to distinguish different magnetic flux bundles. The NLFFF reconstruction gives an MFR structure that is consistent with the hot channel in the EUV images before the eruption at 08:24

UT. The open flux bundles (in Figure 3(c) and (d)) coming from the positive polarity sunspot in the south of the MFR look like a wall inclining to the northeast. The strong magnetic pressure from the positive sunspot may change the propagation direction of the MFR as well as its axis orientation.

We now calculate the magnetic energy density $\varepsilon_B = \mathbf{B}^2/2\mu_0$, using the reconstruction results, where the coronal magnetic field \mathbf{B} is from the NLFFF extrapolation and μ_0 is the vacuum permeability. Figure 4 plots the magnetic energy density distribution around the CME source region overlying the MFR before the eruption at heights of $1.07 R_\odot$ and $1.14 R_\odot$, respectively. The black and white diamonds mark the footpoints of the MFR on the solar surface. The arrow shows the orientation and position of the central part of the MFR before the eruption that likely impact the Earth. The distribution of the magnetic energy density shows a strong gradient descent toward the northeast. Comparing the magnetogram contours in Figure 3(a) with the magnetic energy density distribution at $1.07 R_\odot$, we can see that the peak of the energy density distribution corresponds to the sunspots in the south of the MFR. It suggests that the gradient descent is largely produced by the sunspots in the south of the MFR. The magnetic field surrounding the MFR may influence the propagation direction and axis orientation of the MFR. The present magnetic energy gradient suggest that the erupting MFR would propagate toward the northeast.

3. MFR CHARACTERISTICS IN THE EXTENDED CORONA

During 2015 December 16 CME, the *STEREO A* spacecraft was 166.5° east of the Earth and at a distance of 0.96 AU from the Sun. Communications with *STEREO B* were lost from 2014 October 1. We use the beacon images of *STEREO A* as the science data on 2015 December 16 are not available. The CME is observed as a halo-like CME by *SOHO/LASCO*. In order to determine the propagation direction of the CME and the orientation of the MFR in the extended corona, we employ simultaneous two-point (*STEREO A* and *SOHO/LASCO*) white-light observations with the

graduated cylindrical shell (GCS) model (Thernisien et al. 2006, 2009). It has six free parameters: the longitude and latitude of the propagation direction, the tilt angle of the flux rope, the height of the CME leading front, the half-angle between the two legs of the flux rope, and the aspect ratio of the CME flux rope. The coronagraph observations and the modeling of the CME are displayed in Figure 5. The wireframe rendering obtained from the GCS model is consistent with the observed images from the two viewpoints. The resulting parameters are listed in Table 1. The propagation direction of the CME deviates by about 45° to the east and about 30° to the north from the radial direction of the source region (S15W15). This change is consistent with what the gradient of the coronal magnetic energy distribution predicts. The tilt angle of the MFR from the GCS model is -80° . The axis of the MFR may point to the south or north. In any case, the axis orientation of the MFR has changed in the corona by comparing with the orientation of the MFR in the source region. These results reveal that the rotation and non-radial motion of the CME MFR occurred very close to the sun as suggested by Kay et al. (2013, 2015). Vourlidis et al. (2011) also shows a rotation during the early evolution of the associated CME.

4. MFR CHARACTERISTICS AT 1 AU AND RELATION TO GEOMAGNETIC ACTIVITY

The *in situ* measurements associated with the CME on 2015 December 16 at *Wind* are presented in Figure 6. A shock passed *Wind* at 15:40 UT on 2015 December 19. A magnetic cloud (MC) is identified with the plasma and magnetic field parameters. The magnetic field is measured in RTN coordinates (in which R points from the Sun to the spacecraft, T is parallel to the solar equatorial plane and points to the planet motion direction, and N completes the right-handed triad). The magnetic field strength first increases to about 20 nT and then decreases smoothly. The T component is largely positive, the R component rotates from positive to negative, and the N component rotates from negative to positive. The D_{st} profile indicates a two-step geomagnetic storm sequence with a

global minimum of -155 nT. The first dip is produced by the southward magnetic field component in the sheath region behind the shock, while the second one is caused by the southward field within the MC that is as high as -20 nT and lasts for about 24 hours. The modeled D_{st} index using the O'Brien & McPherron (2000) formula (minimum -156 nT) agrees with the observed D_{st} well, where the Burton et al. (1975) method gives a deeper globe minimum (-244 nT) than observed.

We use a Grad-Shafranov (GS) method (Hau & Sonnerup 1999; Hu & Sonnerup 2002) to reconstruct the MC structure, which has been validated by well-separated, multi-spacecraft measurements (Liu et al. 2008a). The GS reconstruction also helps determine the boundaries of the MC. There is also a significant southward field component ahead of the resulting MC leading edge (see Figure 6). The magnetic field strength, however, is not smooth. The GS method is sensitive to the boundaries. When interval with southward fields starting from about 3:00 UT to 16:00 UT on 2015 December 20 is included, the GS method cannot give a reasonable reconstruction. The reconstruction result are shown in Figure 7. The right-handed flux-rope structure resulting from the GS reconstruction is consistent with the MFR structure in the source region. It has an elevation angle of about -70° and an azimuthal angle of about 100° in RTN coordinates of the Earth. The maximum value of the axial magnetic field is 17.7 nT, comparable to the total magnetic field strength. The axial magnetic field component is the main contributor to the southward magnetic field producing the geomagnetic storm, given the almost southward axis orientation.

Figure 8 shows the axis orientations of the MFR from different observations. The axis elevation angle and azimuthal angle of the MFR at 1 AU are -70° and 100° , respectively (OC in Figure 8). The axis of the MFR at 1 AU largely points southward. If the axial magnetic field did not change its sign during the propagation in the inner heliosphere, the orientation of the MFR from the GCS model would also largely point to the south. The axis orientation of the MFR at 1 AU is thus almost aligned with the orientation of the MFR in the extended corona (OB in Figure 8). Comparing with

the MFR orientation in the source region (OA in Figure 8), we can see that the axis has rotated by about 95° . These results indicate that the rotation of the MFR may have occurred mainly in the low corona. The MFR axis was largely horizontal in the source region but became almost southward in the extended corona and at 1 AU. It is the rotation of the flux rope that has resulted in the intense geomagnetic storm.

5. SUMMARY AND DISCUSSIONS

We have investigated the rotation and non-radial motion of a CME MFR from AR 12468 (S15W15) on 2015 December 16, using the EUV, magnetogram, white-light and *in situ* observations from *SDO*, *SOHO*, *STEREO A*, and *Wind*. We use an NLFFF model to extrapolate the coronal magnetic field around the AR, a GCS method to determine the propagation direction and orientation of the MFR near the Sun, and a GS reconstruction technique to derive the magnetic structure of the MFR at 1 AU and understand its relationship to the geomagnetic activity. The results are summarized and discussed as follows.

1. The CME changed its propagation direction by about 45° in latitude and about 30° in longitude in the low corona due to the asymmetric distribution of the magnetic energy around the source region. We obtain the coronal magnetic field of the AR from the NLFFF method. The open magnetic fields surrounding the MFR incline to the northeast of the source region. In order to evaluate the influence of the magnetic pressure on the CME propagation direction, we analyse the the magnetic energy density distributions at different heights based on the NLFFF extrapolation results. The magnetic energy density distribution on each layer shows a gradient descent toward the northeast of the AR, which is consistent with the CME propagation direction. This indicates that the coronal magnetic field context of the AR plays an important role in the CME propagation direction.

2. The MFR rotated counterclockwise by about 95° in the low corona during the eruption, which,

again, can be attributed to the coronal magnetic field configuration around the AR. The error in the MFR orientation in our case cannot be rigorously determined, but is roughly 20° at the source, 20° in the corona from the GCS method, and 10° - 30° from GS reconstruction. These errors may not affect our conclusion on the MFR rotation here, which is about 95° . Compared with the MFR on the solar surface before eruption, the MFR obtained from the GCS model in white-light observations rotated by about 95° counterclockwise. The near-Earth MFR from GS reconstruction has almost the same orientation as the MFR from the GCS model. The MFR was nearly horizontal in the solar source region, but became largely southward in the extended corona and near the Earth. Therefore, the rotation of the MFR plays an important role in the generation of the intense geomagnetic storm. Previous studies of the kink stability ([Green et al. 2007](#)) and of the magnetic tension force ([Lynch et al. 2009](#)) suggest that the rotation direction of an MFR is determined by the sign of helicity of the source region: the positive (right-handed) ones rotate clockwise while the negative (left-handed) ones rotate counterclockwise. In our case, the MFR is right-hand but rotates counterclockwise. However, the possibility of a clockwise rotation for 265° , which would result in the same orientation as in the extended corona, can not be completely excluded. In any case, the geometry of the MFR in relation to the AR coronal magnetic field context is considered to be an important factor for the rotation.

The research was supported by the Recruitment Program of Global Experts of China, NSFC under grants 41374173, 41774179 and 41604146, and the Specialized Research Fund for State Key Laboratories of China. We acknowledge the use of data from *SOHO*, *STEREO*, *Wind*, *SDO*, and the D_{st} index from WDC in Kyoto.

Table 1. CME Parameters Obtained from the GCS Model.

Time(UT)	Lon($^{\circ}$)	Lat($^{\circ}$)	Tilt Angle($^{\circ}$)	Aspect Ratio	Half Angle($^{\circ}$)	Height (R_{\odot})
11:12	E30.0	N15.0	-80.0	0.4	35.0	10.0
12:30	E30.0	N15.0	-80.0	0.4	35.0	14.0

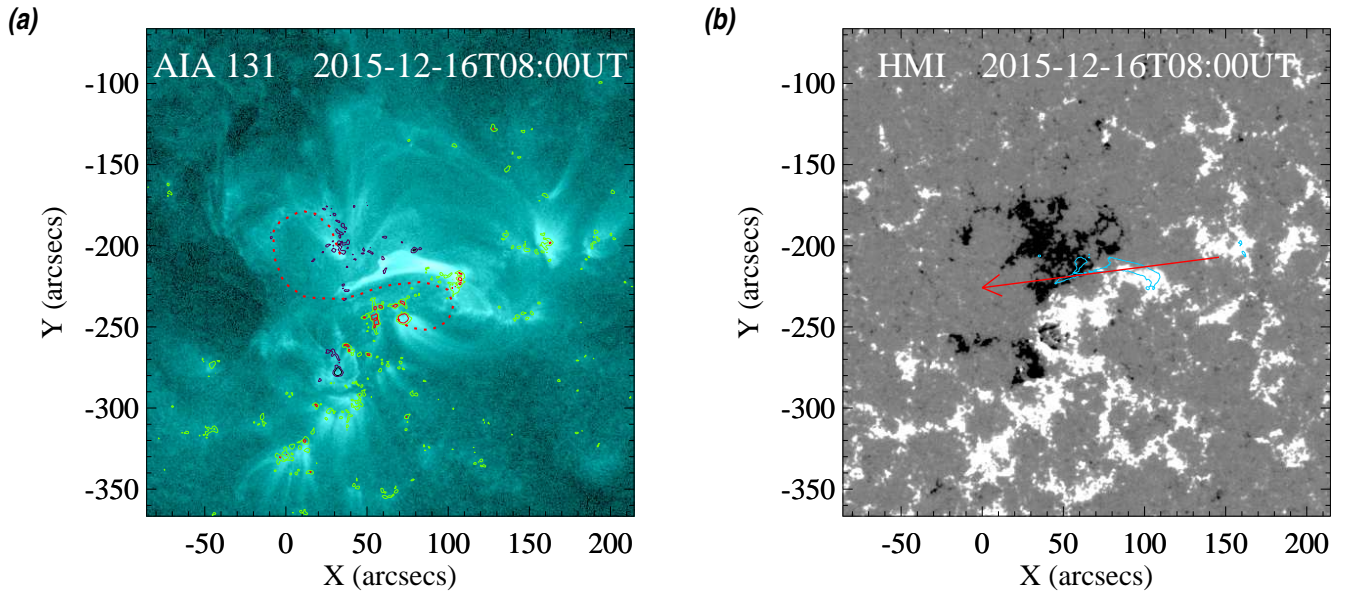


Figure 1. EUV and HMI observations of the source region before the eruption. (a): *SDO/AIA* 131 Å EUV image of source region. The dashed red curve indicates the synoptic configuration of the flux rope. Contours of -800 , -400 , 400 and 800 G of the photospheric magnetic field along the line of sight from a HMI magnetogram is overlaid on the EUV image and are marked in black, blue, green and red, respectively. (b): Line-of-sight magnetogram from *SDO/HMI*. The blue contour indicates the central part of MFR. The red arrow shows the orientation of the central part of the MFR.

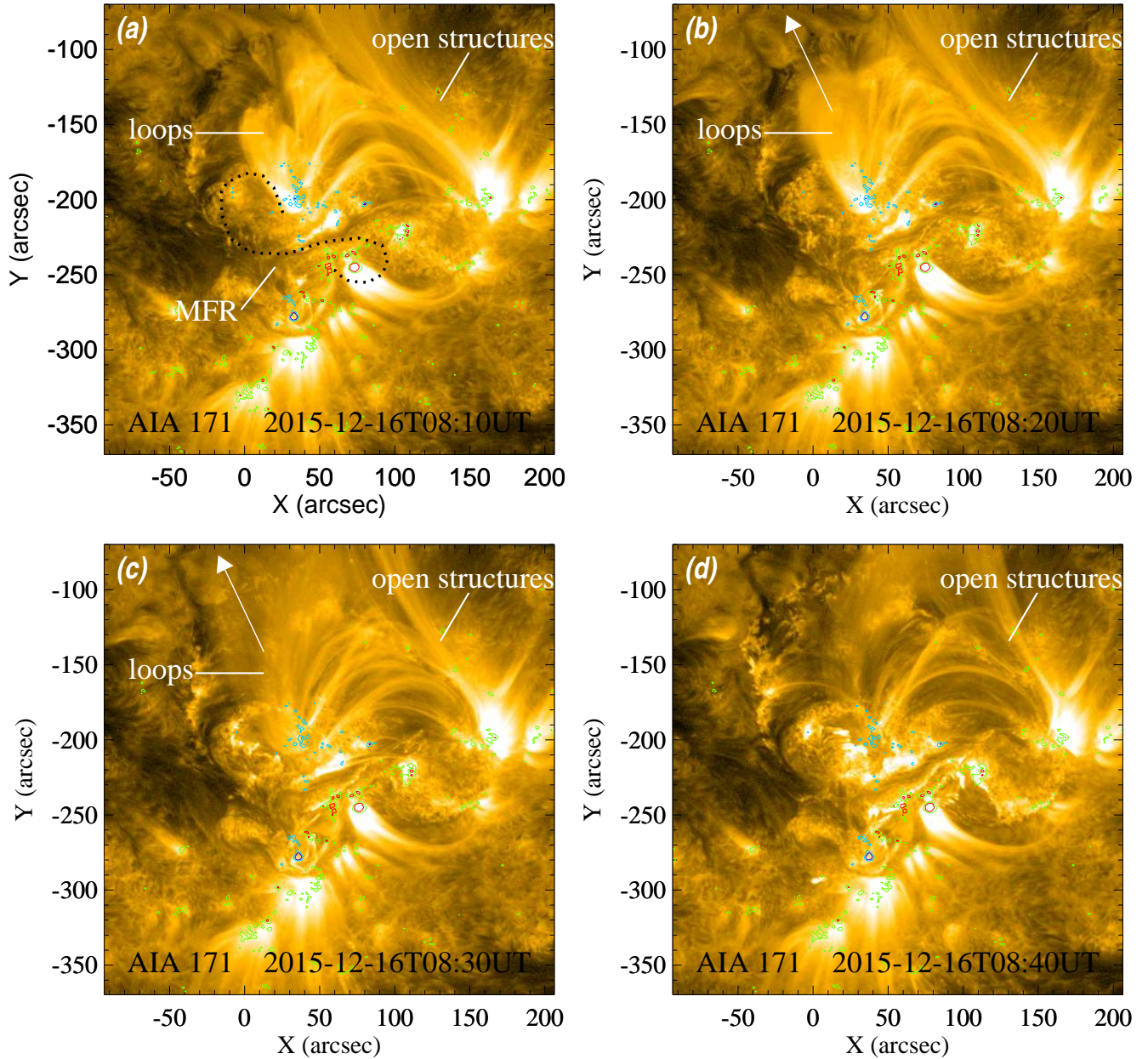


Figure 2. EUV structures and the eruption of the CME MFR in *SDO/AIA* 171 Å at different times. Contours of -800 , -400 , 400 and 800 G of the photospheric magnetic field along the line of sight from HMI magnetograms are overlaid on the EUV images and are marked in blue, cyan, green and red, respectively. The black dotted curve in (a) shows the location of the MFR from *SDO/AIA* 131 Å. The loops overlying the MFR and the open EUV structures surrounding the MFR are marked respectively in (a)-(c). The arrow in (b) and (c) shows the expansion direction of the overlying loops. The open EUV structures are also marked in (d).

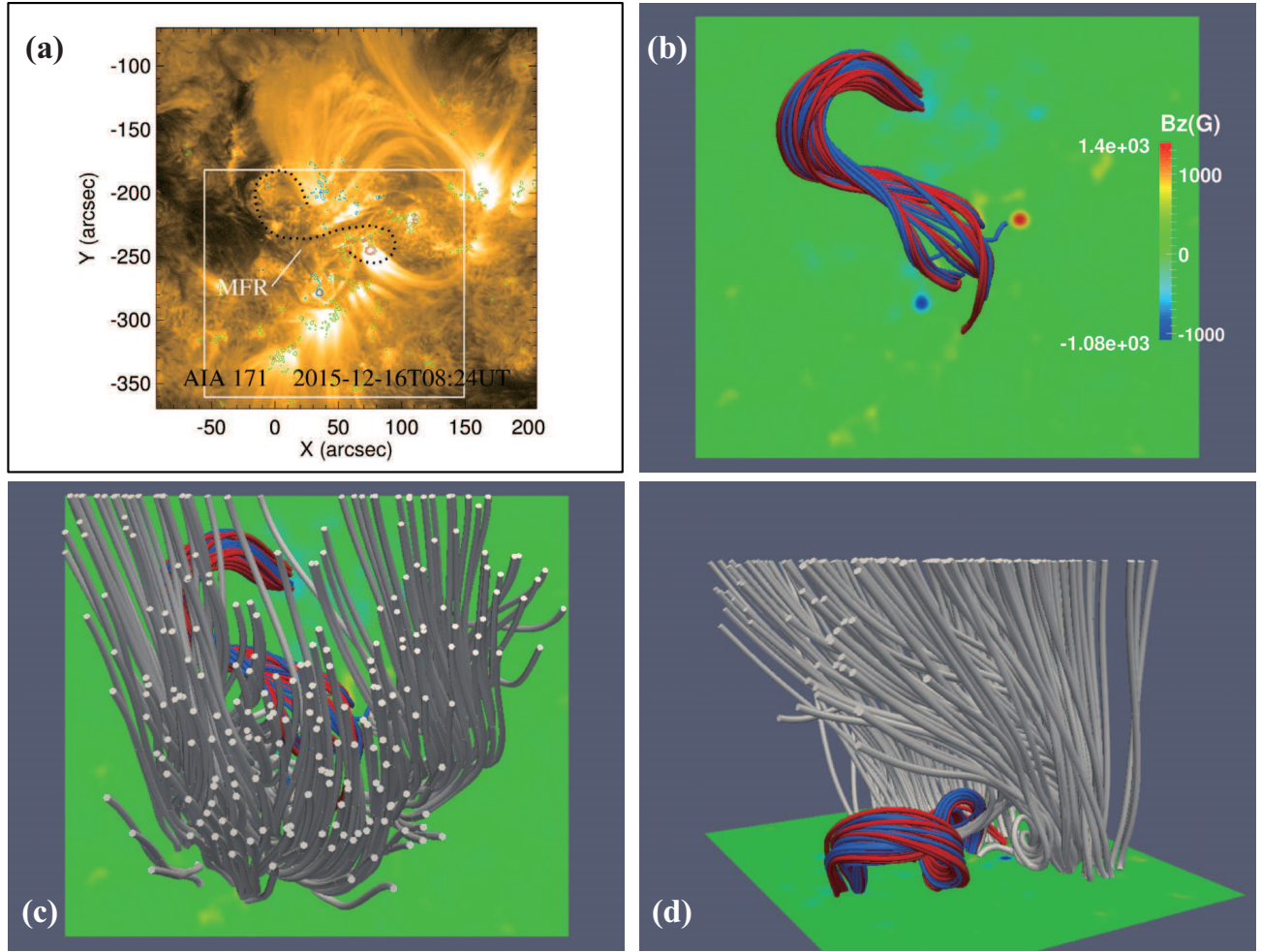


Figure 3. EUV structures of the source region from *SDO/AIA* 171 Å and the NLFFF reconstruction of coronal magnetic fields of the source region at 8:24 UT. (a): Contours of the photospheric magnetic fields are the same as in Figure 2. The white box indicates the reconstruction region for (b)-(d). (b) and (c): The red and blue field lines represent the MFR. The white lines show the open flux bundles. The color bar gives the vertical component of the background magnetic fields of the photosphere. (d): A view from the northeast of the AR.

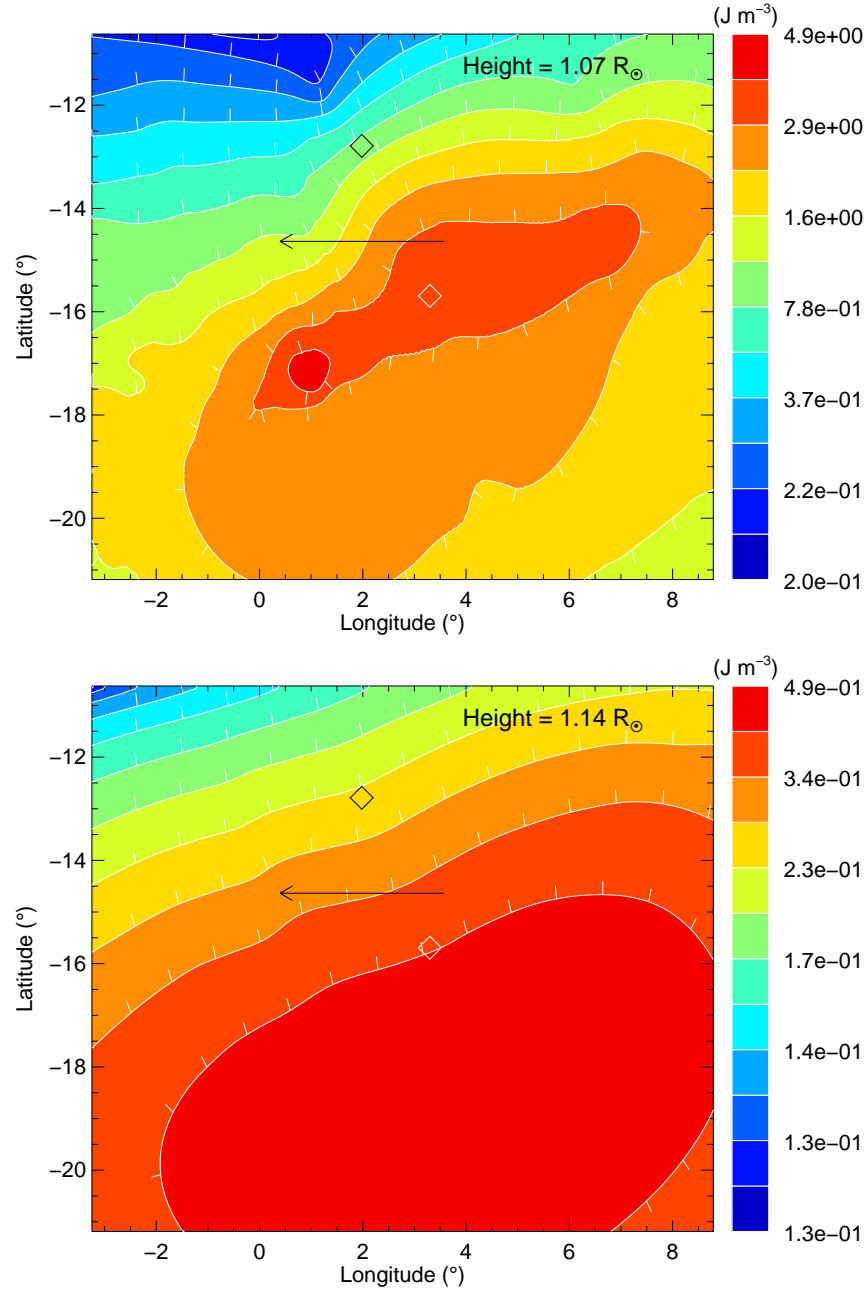


Figure 4. Distribution of the magnetic energy density at the heights of $1.07 R_{\odot}$ (upper panel) and $1.14 R_{\odot}$ (lower panel) based on the NLFFF reconstruction. The black and white diamonds mark the footpoints of the MFR on the solar surface. The arrow shows the orientation of the central part of the MFR before the eruption.

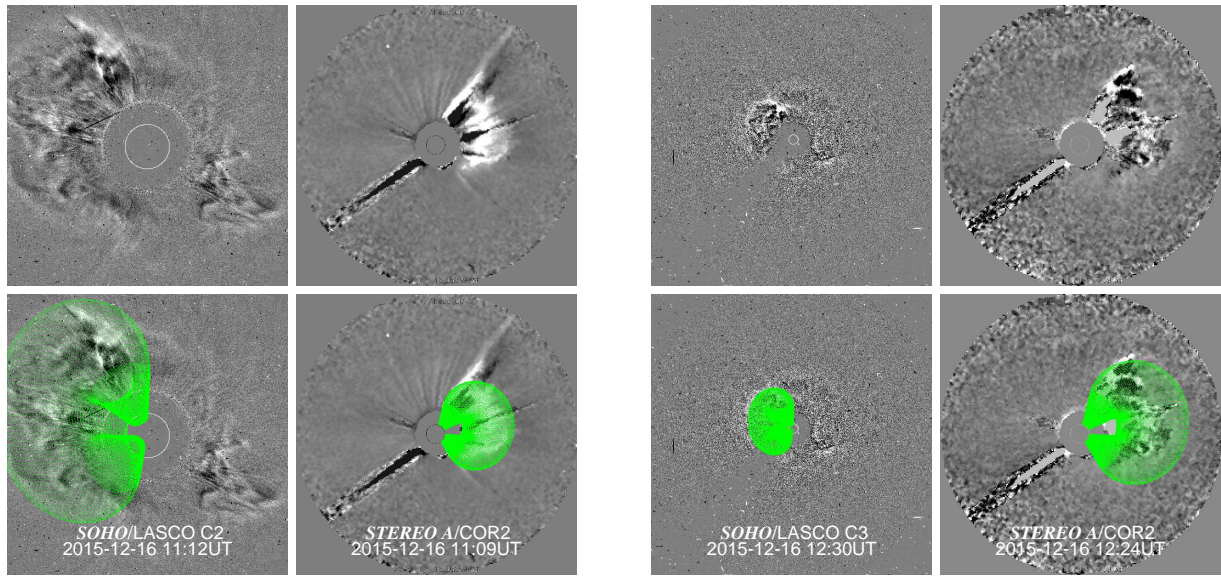


Figure 5. Running difference coronagraph images of the CME from *SOHO/LASCO* and *STEREO A/COR2* (upper) and GCS modeling overlaid on the observed images (bottom). Only two frames are available for *STEREO A/COR2* observations.

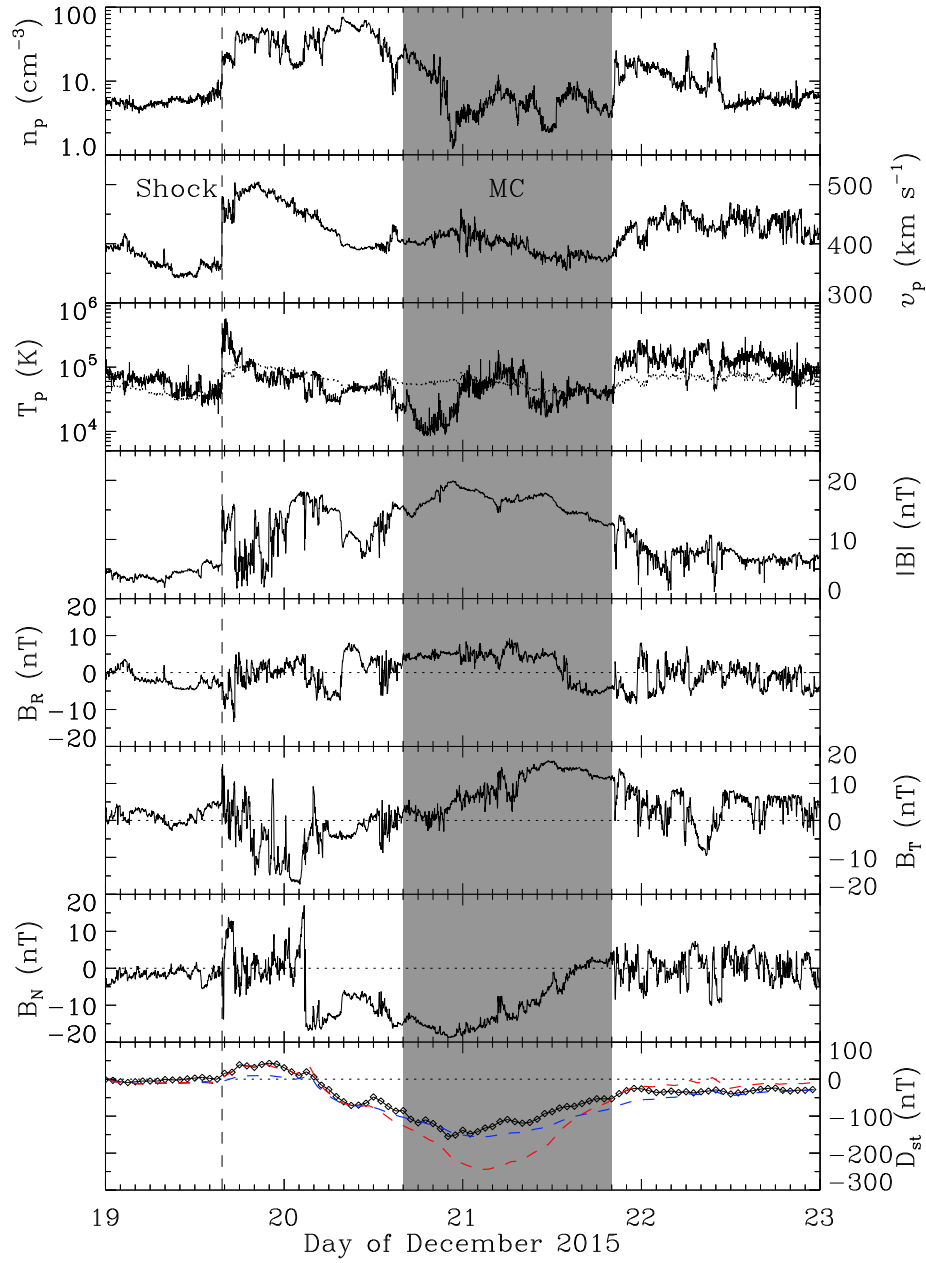


Figure 6. Solar wind plasma and magnetic field parameters associated with the CME at *Wind*. From top to bottom, the panels show the proton density, bulk speed, proton temperature, magnetic field strength and components, and D_{st} index, respectively. The dotted line in the third panel denotes the expected proton temperature calculated from the observed speed (Lopez 1987). The blue and red dashed curves in the bottom panel represent D_{st} values estimated with the southward magnetic field component in GSM coordinates using the formulae of O’Brien & McPherron (2000) and Burton et al. (1975), respectively. The shaded region indicates the magnetic cloud interval determined by the GS reconstruction, and the vertical dashed line marks the associated shock.

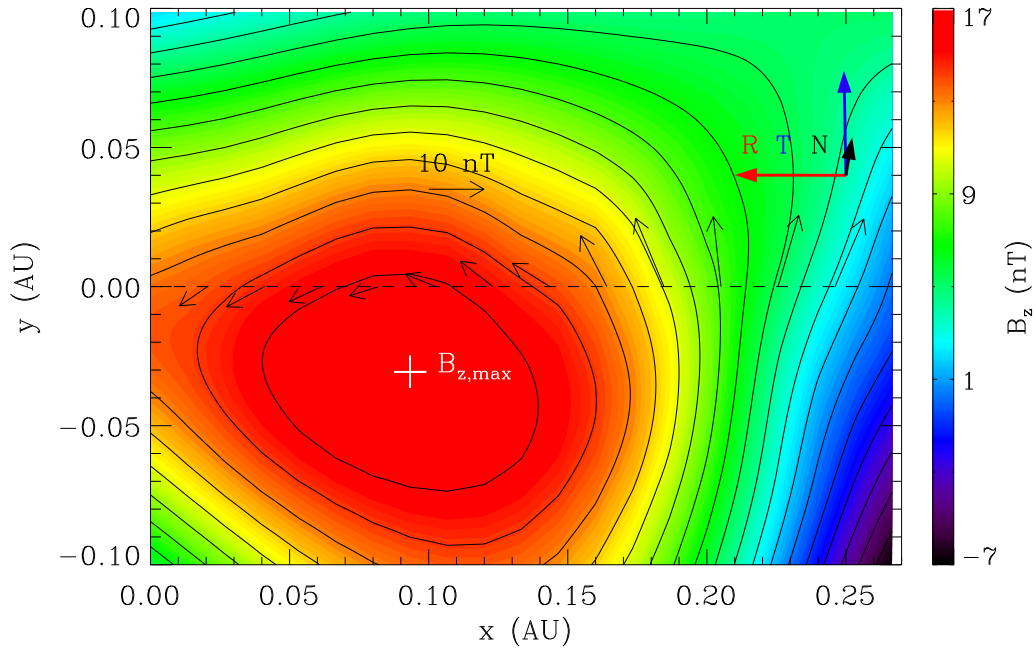


Figure 7. Reconstructed cross section of the magnetic cloud at *Wind*. Black contours show the distribution of the vector potential, and the color shading indicates the value of the axial magnetic field scaled by the color bar on the right. The location of the maximum axial field is indicated by the white cross. The dashed line marks the trajectory of *Wind*. The thin black arrows denote the direction and magnitude of the observed magnetic fields projected onto the cross section, and the thick colored arrows show the projected RTN directions.

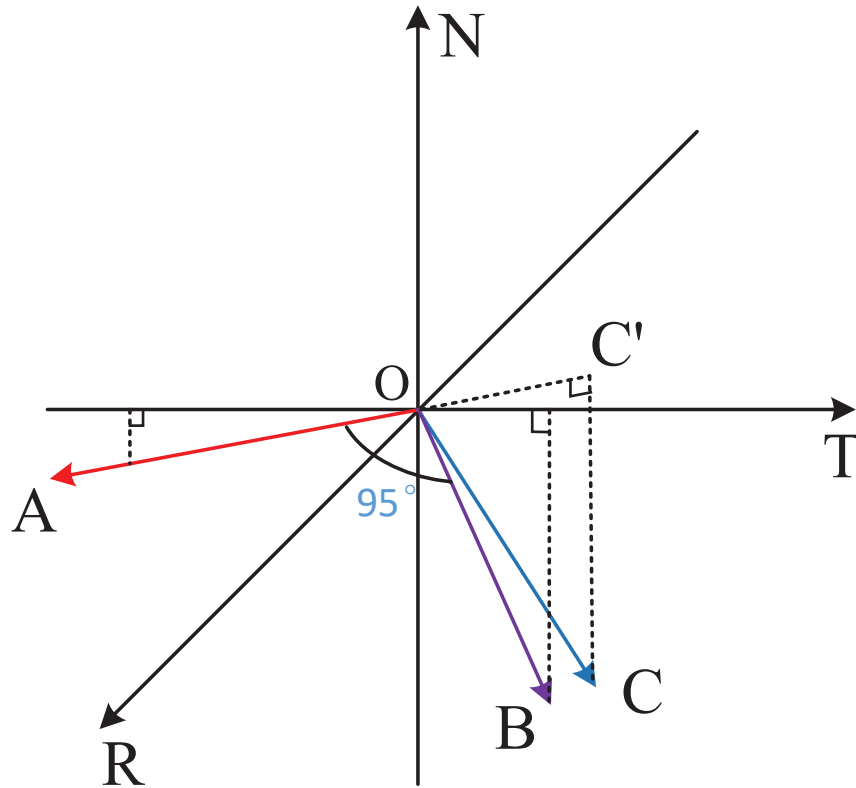


Figure 8. Axis orientations of the flux rope from different observations. The red (OA), purple (OB) and blue (OC) arrows show the orientations of the MFR in the source region, in the extended corona, and at 1 AU in RTN coordinates of the Earth, respectively. OA has an elevation angle of -5° and azimuthal angle of 270° . OB has an elevation angle of -80° and azimuthal angle of 90° . OC has an elevation angle of -70° and azimuthal angle of 100° .

REFERENCES

- Burton, R. K., McPherron, R. L., & Russell, C. T. 1975, *JGR*, 80, 4204
- Canfield, R. C., Hudson, H. S., & McKenzie, D. E. 1999, *GeoRL*, 26, 627
- Cheng, X., Zhang, J., Ding, M. D., Liu, Y., & Poomvises, W. 2013, *ApJ*, 763, 43
- Cheng, X., Ding, M. D., Guo, Y., et al. 2014, *ApJ*, 780, 28
- Cohen, O., Attrill, G. D. R., Schwadron, N. A., et al. 2010, *Journal of Geophysical Research (Space Physics)*, 115, A10104
- Fan, Y., & Gibson, S. E. 2004, *ApJ*, 609, 1123
- Forsyth, R. J., Bothmer, V., Cid, C., et al. 2006, *SSRv*, 123, 383
- Gopalswamy, N., Mäkelä, P., Xie, H., Akiyama, S., & Yashiro, S. 2009, *Journal of Geophysical Research (Space Physics)*, 114, A00A22
- Gopalswamy, N., Yashiro, S., Kaiser, M. L., Howard, R. A., & Bougeret, J.-L. 2001, *ApJL*, 548, L91
- Green, L. M., & Kliem, B. 2014, in *IAU Symposium*, Vol. 300, *Nature of Prominences and their Role in Space Weather*, ed. B. Schmieder, J.-M. Malherbe, & S. T. Wu, 209–214
- Green, L. M., Kliem, B., Török, T., van Driel-Gesztelyi, L., & Attrill, G. D. R. 2007, *SoPh*, 246, 365
- Gui, B., Shen, C., Wang, Y., et al. 2011, *SoPh*, 271, 111
- Guo, Y., Schmieder, B., Démoulin, P., et al. 2010, *ApJ*, 714, 343
- Hau, L.-N., & Sonnerup, B. U. Ö. 1999, *JGR*, 104, 6899
- Hu, H., Liu, Y. D., Wang, R., et al. 2017, *ApJ*, 840, 76
- Hu, Q., & Sonnerup, B. U. Ö. 2002, *JGRA*, 107, 1142
- Illing, R. M. E., & Hundhausen, A. J. 1985, *JGR*, 90, 275
- Isavnin, A., Vourlidas, A., & Kilpua, E. K. J. 2014, *SoPh*, 289, 2141
- Kataoka, R., Shiota, D., Kilpua, E., & Keika, K. 2015, *GeoRL*, 42, 5155
- Kay, C., Opher, M., & Evans, R. M. 2013, *ApJ*, 775, 5
- . 2015, *ApJ*, 805, 168
- Kilpua, E. K. J., Li, Y., Luhmann, J. G., Jian, L. K., & Russell, C. T. 2012, *Annales Geophysicae*, 30, 1037
- Kilpua, E. K. J., Pomoell, J., Vourlidas, A., et al. 2009, *Annales Geophysicae*, 27, 4491
- Kliem, B., Török, T., & Thompson, W. T. 2012, *SoPh*, 281, 137
- Lemen, J. R., Title, A. M., Akin, D. J., et al. 2012, *SoPh*, 275, 17
- Liewer, P., Panasenco, O., Vourlidas, A., & Colaninno, R. 2015, *SoPh*, 290, 3343
- Liu, Y., Luhmann, J. G., Huttunen, K. E. J., et al. 2008a, *ApJL*, 677, L133
- Liu, Y., Thernisien, A., Luhmann, J. G., et al. 2010, *ApJ*, 722, 1762
- Liu, Y., Luhmann, J. G., Müller-Mellin, R., et al. 2008b, *ApJ*, 689, 563
- Liu, Y. D., Hu, H., Wang, C., et al. 2016, *ApJS*, 222, 23
- Liu, Y. D., Luhmann, J. G., Kajdič, P., et al. 2014, *Nature Communications*, 5, 3481
- Lopez, R. E. 1987, *JGR*, 92, 11189
- Lugaz, N., Downs, C., Shibata, K., et al. 2011, *ApJ*, 738, 127
- Lugaz, N., Farrugia, C. J., Davies, J. A., et al. 2012, *ApJ*, 759, 68
- Lynch, B. J., Antiochos, S. K., Li, Y., Luhmann, J. G., & DeVore, C. R. 2009, *ApJ*, 697, 1918
- MacQueen, R. M., Hundhausen, A. J., & Conover, C. W. 1986, *JGR*, 91, 31
- Manchester, W., Kilpua, E. K. J., Liu, Y. D., et al. 2017, *SSRv*, 212, 1159
- Möstl, C., Rollett, T., Frahm, R. A., et al. 2015, *Nature Communications*, 6, 7135
- O'Brien, T. P., & McPherron, R. L. 2000, *JGR*, 105, 7707
- Pesnell, W. D., Thompson, B. J., & Chamberlin, P. C. 2012, *SoPh*, 275, 3
- Savani, N. P., Vourlidas, A., Szabo, A., et al. 2015, *Space Weather*, 13, 374
- Schou, J., Scherrer, P. H., Bush, R. I., et al. 2012, *SoPh*, 275, 229
- Shen, C., Wang, Y., Gui, B., Ye, P., & Wang, S. 2011, *SoPh*, 269, 389
- Thernisien, A., Vourlidas, A., & Howard, R. A. 2009, *SoPh*, 256, 111
- Thernisien, A. F. R., Howard, R. A., & Vourlidas, A. 2006, *ApJ*, 652, 763
- Thompson, W. T. 2011, *Journal of Atmospheric and Solar-Terrestrial Physics*, 73, 1138
- Thompson, W. T., Kliem, B., & Török, T. 2012, *SoPh*, 276, 241
- Török, T., & Kliem, B. 2003, *A&A*, 406, 1043
- . 2005, *ApJL*, 630, L97
- Vemareddy, P., Ambastha, A., & Wiegelmann, T. 2013, *Bulletin of the Astronomical Society of India*, 41, 183
- Vemareddy, P., Cheng, X., & Ravindra, B. 2016, *ApJ*, 829, 24
- Vourlidas, A., Colaninno, R., Nieves-Chinchilla, T., & Stenborg, G. 2011, *ApJL*, 733, L23
- Vourlidas, A., Lynch, B. J., Howard, R. A., & Li, Y. 2013, *SoPh*, 284, 179
- Wang, R., Liu, Y. D., Dai, X., et al. 2015, *ApJ*, 814, 80
- Wang, R., Liu, Y. D., Yang, Z., & Hu, H. 2014, *ApJ*, 791, 84
- Wheatland, M. S., Sturrock, P. A., & Roumeliotis, G. 2000, *ApJ*, 540, 1150
- Wiegelmann, T. 2004, *SoPh*, 219, 87
- Wiegelmann, T., & Inhester, B. 2010, *A&A*, 516, A107
- Wiegelmann, T., Thalmann, J. K., Inhester, B., et al. 2012, *SoPh*, 281, 37
- Yurchyshyn, V. 2008, *ApJL*, 675, L49
- Yurchyshyn, V., Abramenko, V., & Tripathi, D. 2009, *ApJ*, 705, 426
- Zhang, J., Cheng, X., & Ding, M.-D. 2012, *Nature Communications*, 3, 747